Full Length Article

Unlocking the role of Ni-Fe species in CO_2 methanation

Penghui Yan [a], Hong Peng [a,*], Xi Zhang [a], Hesamoddin Rabiee [a,b], Mohamed Ahmed [a], Yilun Weng [c], Alexandra Rozhkovskaya [d], John Vogrin [d], Muxina Konarova [a], Zhonghua Zhu [a,*]

[a] *School of Chemical Engineering, The University of Queensland, St Lucia, QLD 4072, Australia*
[b] *Centre for Future Materials, University of Southern Queensland, Springfield, QLD 4300, Australia*
[c] *Australian Institute for Bioengineering and Nanotechnology, The University of Queensland, St Lucia, 9 QLD 4072, Australia*
[d] *Zeotech Limited, Brisbane Technology Park, QLD, Eight Mile Plains 4113, Australia*

ABSTRACT

The conversion of CO_2 to methane has garnered immense interest, owing to its pivotal roles in reducing carbon emissions and producing environmentally friendly natural gas. This study explores the application of 13X zeolite-supported Ni-Fe catalysts with varying Ni/Fe ratios in CO_2 methanation. Structural analyses reveal the formation of Ni-Fe alloy species. Specifically, the Ni-Fe species induce a high binding energy shift for Fe and a low energy shift for Ni species. Additionally, the presence of Ni-Fe species results in a slight increase in the reduction temperature for Ni species, while significantly lowering the reduction temperature of Fe species. Comparative assessments demonstrate that Ni-Fe species exhibit diminished hydrogenation activity in comparison to mono-metallic Ni species, resulting in reduced CO_2 conversion and CH_4 selectivity with increased Fe/Ni ratios. Notably, 5Ni-5Fe-13X and 2Ni-8Fe-13X catalysts display heightened activity in the conversion of CO_2 to CO and ethane. Furthermore, this study finds that the blockage of micropores does not significantly affect the catalyst's methanation activity, suggesting the small metal species in the micropores did not promote the CO_2 methanation activity. In situ DRIFTS reveals that the formate intermediate is promoted by the presence of Ni species, whereas the formation of CO intermediate is facilitated by Ni-Fe species. These insights deepen our grasp of the structural and catalytic attributes inherent to Ni-Fe species in the context of CO_2 conversion, fostering a more comprehensive understanding of their functionality in this critical process.

1. Introduction

Renewable energy sources, such as biomass, wind and solar, provide a sustainable solution to the ever-growing demand for energy [1–4]. Synthetic natural gas (SNG) produced within the power-to-gas process is a promising and suitable chemical energy carrier due to its long-term storage ability and the existing infrastructure in the form of the natural gas grid [5]. Within the power-to-gas process chain, green H_2 generated from excess renewable electric power and CO_2 released from industry are catalytically converted to methane via Sabatier reaction (Eq.1) [6,7]. While CO_2 methanation is thermodynamically favourable [8], this reaction requires to reduce the fully oxidized carbon into methane, which is an eight-electron process with significant kinetic limitations [9]. Therefore, high temperature is required to activate the inert CO_2 molecule [10,11].

$$CO_2 + 4H_2 \rightarrow CH_4 + 2H_2O \tag{1}$$
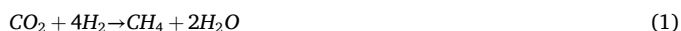
The employment of catalysts is instrumental in reducing the activation energy required for CO_2 methanation. As a result, various metals are utilized to enhance the efficiency of CO_2 methanation processes. The activity of metallic centers for the methanation reaction to be correlated as follows: Ru > Ni > Fe > Co > Os > Pt > Ir > Mo > Pd [12,13]. Ni metal is the state-of-the-art catalysts for CO_2 methanation due to its high activity, high selectivity and relatively low cost, rendering it attractive for industrial-scale applications [14–18]. Fe catalysts have also been investigated for CO_2 methanation as an alternative to Ni, due to its cost and natural abundance [19]. In Kirchner's study [20], nano-sized γ-Fe_2O_3 was explored for CO_2 methanation, demonstrating notable CO_2 activity with a CH_4 yield of 59 % at 400 °C and a H_2/CO_2 molar ratio of 200. Notably, the γ-Fe_2O_3 and α-Fe_2O_3 catalysts exhibited pronounced carbon deposition. The presence of surface carbon species in γ-Fe_2O_3 enhanced CO_2 methanation activity, while bulk carbon and iron carbides over α-Fe_2O_3 impeded CH_4 formation. 13X-supported Fe

catalysts with varying Fe loading were also investigated for CO_2 methanation [21]. Low Fe loading facilitated enhanced metal dispersion, promoting CH_4 formation. Conversely, high Fe loading favoured the development of a Fe_3C shell, thus promoting the production of Fischer-Tropsch products (C_1-C_{80} hydrocarbons) [22]. Despite these variations, all Fe-based catalysts exhibited significantly lower CO_2 conversion (<1%), indicating weak methanation activity compared to monometallic Ni species.

The addition of a second metal (Fe [23], Zr [24], Zn [25], Mn [26], La [27], Mo [28], Cu [29,30], Co [31,32], Ce [33–35], Y [36], La [37]) can improve the catalytic performance and stability due to the improved Ni dispersion and reducibility, increased CO_2 adsorption and high oxygen capacity [38–40]. Zeolites supported nickel–iron catalysts are widely used for a number of reactions due to the well balanced hydrogenation and hydrogenolysis activities [41,42]. It has been reported that Ni-Fe catalysts exhibited an improved CO_2 methanation activity due to an improved CO dissociation [43,44], CO_2 adsorption [45,46] and an improved long-term stability [47]. The bimetallic Ni-Fe catalysts, supported on Al_2O_3, ZrO_2, TiO_2 and SiO_2, demonstrated an elevated CH_4 yield compared to monometallic Ni catalysts [5,48–50]. This improvement was attributed to the formation of a Ni-Fe alloy at a Ni/Fe ratio of 3. The Al_2O_3 supported 17 wt% Ni_3Fe catalyst exhibited a remarkable CO_2 conversion of 71 %, along with 98 % CH_4 selectivity at 358 °C and 6 bar operating conditions [47]. However, the deactivation of Ni_3Fe/Al_2O_3 catalyst occurred in the low-temperature regime, resulting in a shift in product selectivity towards CO and the formation of carbon.

In a study by Serrer [51], the combined X-ray absorption spectroscopy and XRD characterizations were used to investigate the influence of Ni-Fe structures on the stability of CO_2 methanation. The Ni^0 sites were found to be prone to oxidation, leading to catalyst deactivation. However, the edges/corners of the Ni^0 particles played a role in facilitating re-reduction. The addition of sacrificial Fe species was observed to protect Ni from oxidation, as Fe itself exhibited greater dynamism in oxidation, thus preserving the active catalytic species and preventing deactivation. Furthermore, it was reported that Fe can enhance metal dispersion and the adsorption ability of CO_2 and CO, thereby improving CO_2 methanation activity [23]. However, some studies indicated that the modification of Ni with a small amount of Fe species negatively influenced CO_2 methanation, resulting in a significant drop in CO_2 conversion and an increase in CO selectivity [52,53]. This was attributed to the presence of oxidized Fe species in the activated catalysts, weakening the interaction between the metal and intermediate CO, facilitating CO desorption, and leading to higher CO selectivity [53].

Conflicting results exist in the literature regarding the influence of Ni/Fe species on CO_2 methanation activity and product distribution. To address this uncertainty, our study employed 13X-supported Ni-Fe catalysts with varying Ni/Fe ratios for CO_2 methanation. The impact of these ratios on the structure of metal species and 13X zeolite was thoroughly examined using scanning transmission electron microscopy, X-ray photoelectron spectroscopy, temperature-programmed desorption, X-ray diffraction, and BET surface area analyses. Furthermore, the role of the Ni/Fe ratio in CO_2 methanation was explored in a continuous flow reactor under atmospheric pressure, with product analysis performed using an online gas chromatograph and in-situ mass spectrometer. This comprehensive approach aims to provide a clearer understanding of the intricate relationship between Ni/Fe ratios and the catalytic performance in CO_2 methanation. The findings suggest that the inclusion of Fe hampers the hydrogenation activity of Ni, resulting in decreased CO_2 conversion and CH_4 selectivity. In contrast, 5Ni-5Fe-13X and 2Ni-8Fe-13X catalysts facilitate the generation of CO and C_2H_6. Additionally, we show that metal sites within micropores have minimal impact on CO_2 methanation activity. Moreover, the presence of Ni species promotes formate pathways, while Ni-Fe species facilitate CO reaction pathways based on the in-situ diffuse reflectance infrared Fourier Transform spectroscopy (DRIFTS) studies.

2. Experimental section

2.1. Catalyst preparation

13X zeolite purchased from Sigma-Aldrich was used as the substrate. The 13X zeolite supported nickel and iron catalysts were meticulously prepared via a co-impregnation method. To do this, a predetermined mass of nickel nitrate hexahydrate ($Ni(NO_3)_2·6H_2O$, p.a., $\geq$ 98.5 %) and Iron(III) nitrate nonahydrate ($Fe(NO_3)_3·9H_2O$, p.a., $\geq$ 98 %), supplied by Sigma-Aldrich, were dissolved in distilled water to form a solution with varying Ni/Fe ratios. This solution was then impregnated onto precalcined 13X zeolite (450 °C for 2 h). The resulting wet solids were dried at 100 °C for 6 h, followed by calcination in air at 450 °C for 2 h. The catalysts were systematically coded as 10Ni-13X, 8Ni-2Fe-13X, 5Ni-5Fe-13X, 2Ni-8Fe-13X and 10Fe-13X.

2.2. Catalyst characterization

The X-ray powder diffraction (XRD) patterns were obtained in the 2θ range of 5-90° using a Bruker D8 advance diffractometer operating with Cu Kα radiation (40 kV, 40 mA). X-ray photoelectron spectroscopy (XPS) spectra were acquired from a Kratos Axis Ultra XPS featuring a 165 mm hemispherical electron energy analyzer and a monochromatic Al Kα (1486.6 eV) radiation source at 15 kV (10 mA). CASA® software, calibrated to the C1s signal at 284.8 eV, was employed for XPS data analysis. The Ni and Fe contents were determined using inductively coupled plasma atomic emission spectroscopy (ICP-OES).

Nitrogen adsorption–desorption isotherms were investigated at −196 °C using a Micromeritics TriStar II surface area analyzer to assess the surface area and pore properties of the samples. Before nitrogen adsorption, the sample underwent a vacuum heating process at 200 °C for 8 h using a Micromeritics VacPrep 061 sample preparation device. The *t*-plot and Barrett-Joyner-Halenda (BJH) models were utilized to determine the volume, surface area of micro- and *meso*-pores, and pore diameter.

Scanning Transmission electron microscopy (STEM) imaging was conducted using a field emission transmission electron microscope (HF5000) equipped with energy-dispersive X-ray spectroscopy (EDS). Sample preparation involved the ethanol dispersion method, and the samples were placed on a copper grid.

Temperature-programmed desorption (TPD) of CO_2 was conducted using BELCAT-B. The samples underwent reduction with pure H_2 (50 mL/min) at 500 °C for 2 h before adsorption. Subsequently, they were exposed to a flow of CO_2 (20 mL/min) at 50 °C for 20 min, and signals from the thermal conductivity detector (TCD) were recorded from 50 to 600 °C under a flow of He gas (20 mL/min).

Temperature-programmed reduction (TPR) was also performed using BELCAT-B to assess the catalyst's reducibility. The catalyst was initially activated in He (20 mL/min) at 500 °C for 30 min to eliminate water and other impurities, followed by cooling to 50 °C. Reduction was conducted using an H_2 flow (30 mL/min) from 50 °C to 850 °C with a heating rate of 10 °C/min. TCD recorded the hydrogen consumption.

ATR-FTIR analyses were measured with Spectrum 100 FT-IR spectrometer (PerkinElmer) at atmosphere pressure and room temperature. The samples were pressed onto the diamond internal reflection element of the ATR accessory. PerkinElmer TGA 4000 instrument was employed to analysis of the weight loss behaviour of spent catalyst. The sample underwent in situ drying at 100 °C for 30 min in a flowing air gas environment (10 mL/min). Subsequently, it was subjected to a ramp rate of 10 °C/min, reaching a maximum temperature of 800 °C, all while maintaining a continuous air gas flow of 10 mL/min.

In situ DRIFTS experiments were conducted using a Thermo-Fisher Nicolet iS50 FT-IR spectrometer, equipped with MCT detector cooled by liquid nitrogen, and a Harrick Scientific DRIFTS cell with ZnS windows. The FTIR spectra were recorded in the range of 650–4000 cm^{-1}, with 32 scans accumulated at a resolution of 4 cm^{-1}. Approximately 44

mg of the sample was placed in the in situ DRIFTS cell. The sample was reduced at 500 °C in a flow of H_2 (50 sccm) for 2 h, then cooled to 150 °C, and the background spectrum was collected. The reaction gas composition was 20 vol% CO_2 and 80 vol% H_2.

2.3. Catalyst test

The catalytic tests were conducted in a continuous flow reactor under atmospheric pressure. Prior to the tests, samples were pre-reduced at 500 °C for 2 h. Reactivity tests utilized a feed consisting of H_2 and CO_2 at a molar ratio of 4:1, with a total flow of 100 mL·min^{-1}, controlled by Brooks mass flow controllers. The mass of catalyst and gas hourly space velocity (GHSV) remained constant at 30,000 mL h^{-1}·g_{cat}^{-1} for catalytic tests. Reaction temperatures ranged from 350 to 400 °C. A gas mixture of 19 % CO_2, 4 % N_2, and 77 % H_2 from Coregas was used for stability tests.

Analysis of CO, CH_4, C_2H_6 and CO_2 concentrations was performed using an online 2014 Shimadzu Gas Chromatograph (GC) equipped with a ShinCarbon column (2 m, argon as a carrier gas), TCD, and flame ionization detector (FID). BELMass spectrometry was employed to determine the time-on-stream intensity of CH_4 (m/z = 16), CO (m/z = 28), CO_2 (m/z = 44), and C_2H_6 (m/z = 30). CO, CH_4 and C_2H_6 were the identified products in the CO_2 hydrogenation process.

The definitions for CO_2 conversion, CO selectivity, CH_4 and C_2H_6 selectivity are provided below:

$$X_{CO2} = \frac{n_{CO2in} - n_{CO2out}}{n_{CO2in}} \times 100\%$$

$$S_{CO} = \frac{n_{COout}}{n_{CO2in} - n_{CO2out}} \times 100\%$$

$$S_{CH4} = \frac{n_{CH4out}}{n_{CO2in} - n_{CO2out}} \times 100\%$$

$$S_{C2H6} = \frac{n_{C2H6out}}{n_{CO2in} - n_{CO2out}} \times 100\%$$

3. Results and discussion

3.1. The structure characterization of catalysts

The porosity characteristics of the reduced catalysts were evaluated through N_2 adsorption and desorption, with the results summarized in

Table 1
Textural properties of 13X zeolite supported Ni-Fe catalysts.

Catalyst	Ni content[a] (wt%)	Fe content[a] (wt%)	S-micro[b] (m²/g)	S-meso[c] (m²/g)	V-micro[b] (cm³/g)	V-meso[c] (cm³/g)
13X	0	0	567	36	0.29	0.030
10Ni-13X	8.4	0	354	25	0.18	0.017
8Ni-2Fe-13X	6.8	1.6	293	38	0.15	0.035
5Ni-5Fe-13X	4.4	4.2	188	35	0.10	0.035
2Ni-8Fe-13X	1.7	7.1	27	38	0.01	0.030
10Fe-13X	0	9.9	0	24	0	0.019

[a] The Ni and Fe contents of catalysts were obtained from ICP-OES analysis.
[b] From N_2 adsorption measurements (t-plot). S-micro = micropore surface area. V-micro = micropore volume.
[c] From N_2 adsorption measurement (BJH method, 1.7–300 nm), S-meso = mesopore surface area. V-meso = mesopore volume.

Table 1 and Fig. 1a. Type I isotherms were consistently observed over all 13X-based catalysts, suggesting microporous materials. This characteristic can be attributed to the 13X structure, characterized by a cubic faujasite-type framework in the space group Fd-3 m and ring-sizes of 12, 6, and 5 T-atoms [54]. The micropore surface area and volume exhibited a decline with increasing Fe/Ni ratios, suggesting an increased adsorption of Fe species into the pores. Franken [21] also noted the preferential placement of Fe species in octahedral sites within the zeolites.

XRD patterns of the reduced catalysts are illustrated in Fig. 1b and Figure S1. The intensity of 13X diffractions diminished with increasing Fe/Ni ratios (Figure S1), indicative of the pronounced impact of added Fe species on zeolite diffraction. This influence could be attributed to the finely dispersed Fe species on the zeolite surface, disrupting the crystal structure of 13X zeolite. Additionally, the presence of metallic Ni (1 1 1) and Ni (2 0 0) diffractions are notable in the reduced 10Ni-13X catalyst [55], indicating the formation of large Ni nanoparticles. These Ni diffractions decreased with increasing Fe/Ni ratios. However, the detection of Fe diffraction (1 1 0) was exclusive to the reduced 10Fe-13X catalyst and were notably absent in the reduced bimetallic 8Ni-2Fe-13X, 5Ni-5Fe-13X, and 2Ni-8Fe-13X catalysts. This could be due to the formation of small-size Fe species and Ni-Fe particles beyond the detection limit of XRD. The STEM and EDS mappings of the reduced catalysts are depicted in Fig. 1c-g and Figure S2. Substantial agglomerates of large Ni particles are detected primarily on the external surface of 13X zeolite over 10Ni-13X catalyst. Conversely, the metal particles over 5Ni-5Fe-13X and 2Ni-8Fe-13X are distributed in smaller sizes, indicating that the addition of Fe species promotes the uniform distribution of Ni species on 13X zeolite. The d-spacing of 0.204 nm in Fig. 1c2 and 0.200 nm in Fig. 1g2 could be ascribed to the crystal planes of Ni (1 1 1) and Fe (1 1 0) [56]. This observation aligns with the findings from the XRD analysis. The 5Ni-5Fe-13X with d-spacing 0.201 nm and 0.179 nm (Fig. 1e2) could be ascribed to crystal planes of Ni_xFe_y (1 1 1) and Ni_3Fe (2 0 0), respectively [57,58].

The CO_2 adsorption activity of the catalysts was evaluated using temperature-programmed desorption. As depicted in Fig. 2a, the introduction of Ni species resulted in a decrease in the CO_2 adsorption activity of 13X. Notably, the addition of Fe significantly diminished the CO_2 adsorption activity of 13X compared to Ni species. This can be attributed, in part, to the reduction in pore surface area and volume within 13X with high Fe content, as indicated by Fig. 1a.

The reduction activity of Ni and Fe species was explored through H_2-TPR (as shown in Fig. 2b). In the Ni-13X catalyst, reduction peaks at 368 °C and 577 °C were identified. These peaks correspond to the reduction of bulk NiO nanoparticles and small nanoparticles interacting with the support, respectively [59,60]. The reduction profile of 10Fe-13X exhibited two distinct peaks around 498 °C and 866 °C. These can be attributed to the reduction of Fe^{3+} to Fe^{2+} and the subsequent reduction of Fe^{2+} to Fe^0, respectively [41,42]. Notably, with increased Fe contents, the reduction of Ni species exhibited a slight shift to a higher temperature. Conversely, the reduction temperature of Fe species decreased, particularly evident in the 2Ni-8Fe-13X and 5Ni-5Fe-13X catalysts. These findings indicate that the introduction of Fe species to Ni leads to a slight increase in the reduction temperature of Ni species. Concurrently, there is a significant decrease in the reduction temperature of Fe species, suggesting the electron interaction between Ni and Fe species and the formation of Ni-Fe alloy.

The XPS spectra of catalysts were investigated, with the raw data curves shown in Fig. 2c and 2e, and the fitted curves displayed in Fig. 2d and 2f. In the 10Ni-13X catalyst, two prominent peaks at 853.7 eV and 856.2 eV correspond to NiO and Ni(OH)$_x$ [42,61,62]. It is noteworthy that the binding energy of NiO and Ni(OH)$_2$ over 8Ni-2Fe-13X, 5Ni-5Fe-13X, and 2Ni-8Fe-13X shifted to lower values compared to 10Ni-13X, suggesting an increased electron transfer from Fe to Ni species. In 10Fe-13X, the main peak centred at 710.6 eV was attributed to FeO_x $2p_{3/2}$ [63]. With the increase in Ni content, this peak shifts to higher binding energy, indicating a more efficient transfer of electrons from Fe
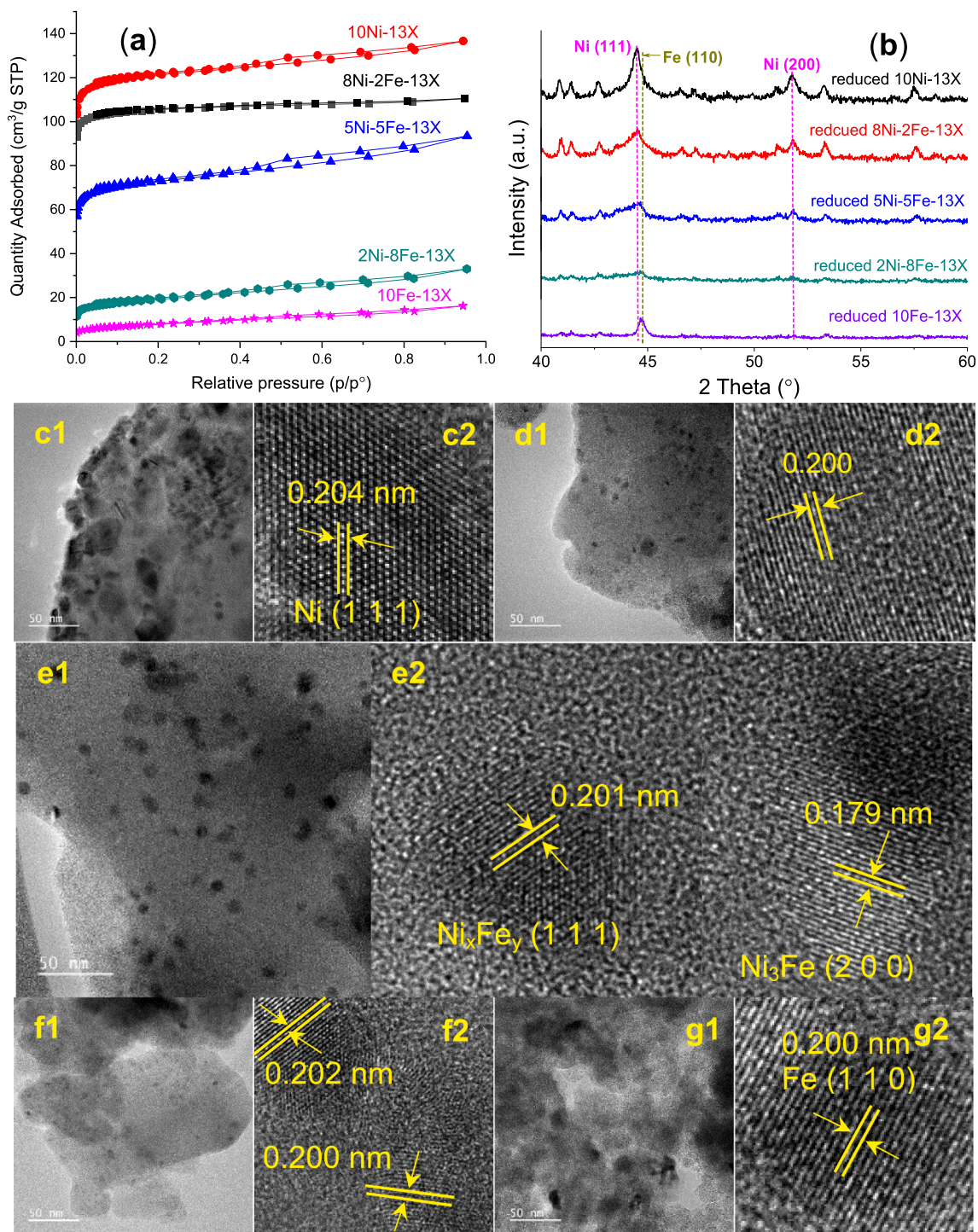
Fig. 1. (**a**) N$_2$ adsorption–desorption isotherms of 13X supported Ni-Fe catalysts. (**b**) XRD patterns of reduced catalysts; TEM images of (**c**) 10Ni-13X, (**d**) 8Ni-2Fe-13X, (**e**) 5Ni-5Fe-13X, (**f**) 2Ni-8Fe-13X, (**g**) 10Fe-13X.

to Ni species. This observation is consistent with the trends observed in the Fe 2p$_{3/2}$ spectra. The electron interaction between Ni and Fe suggests the formation of Ni-Fe alloy species over the bimetallic Ni-Fe catalysts [41]. In Frontera studies [64], it was observed that the augmentation of Fe content (2Ni-8Fe-13X) resulted in a heightened fraction of low valence state Ni species (852.5 eV), suggesting an electron transfer that enhanced the electronegativity of Ni. The introduction of Fe also elevates the surface oxygen content owing to the facile oxidation of Fe species [65]. Furthermore, the oxygen species provided by Fe can migrate to the surface of Ni atoms, potentially diminishing the

hydrogenation activity of Ni. This result aligns with the findings of the H$_2$-TPR analysis, indicating that the addition of Fe lowers the reduction temperature of Fe but raises it for Ni species. The elevated reduction temperature observed for Ni species may be attributed to the migration of oxygen species from Fe to Ni.

3.2. Performance results

The prepared catalysts were tested in a continuous flow reactor for CO$_2$ methanation. As depicted in Fig. 3a, 10Ni-13X demonstrated the
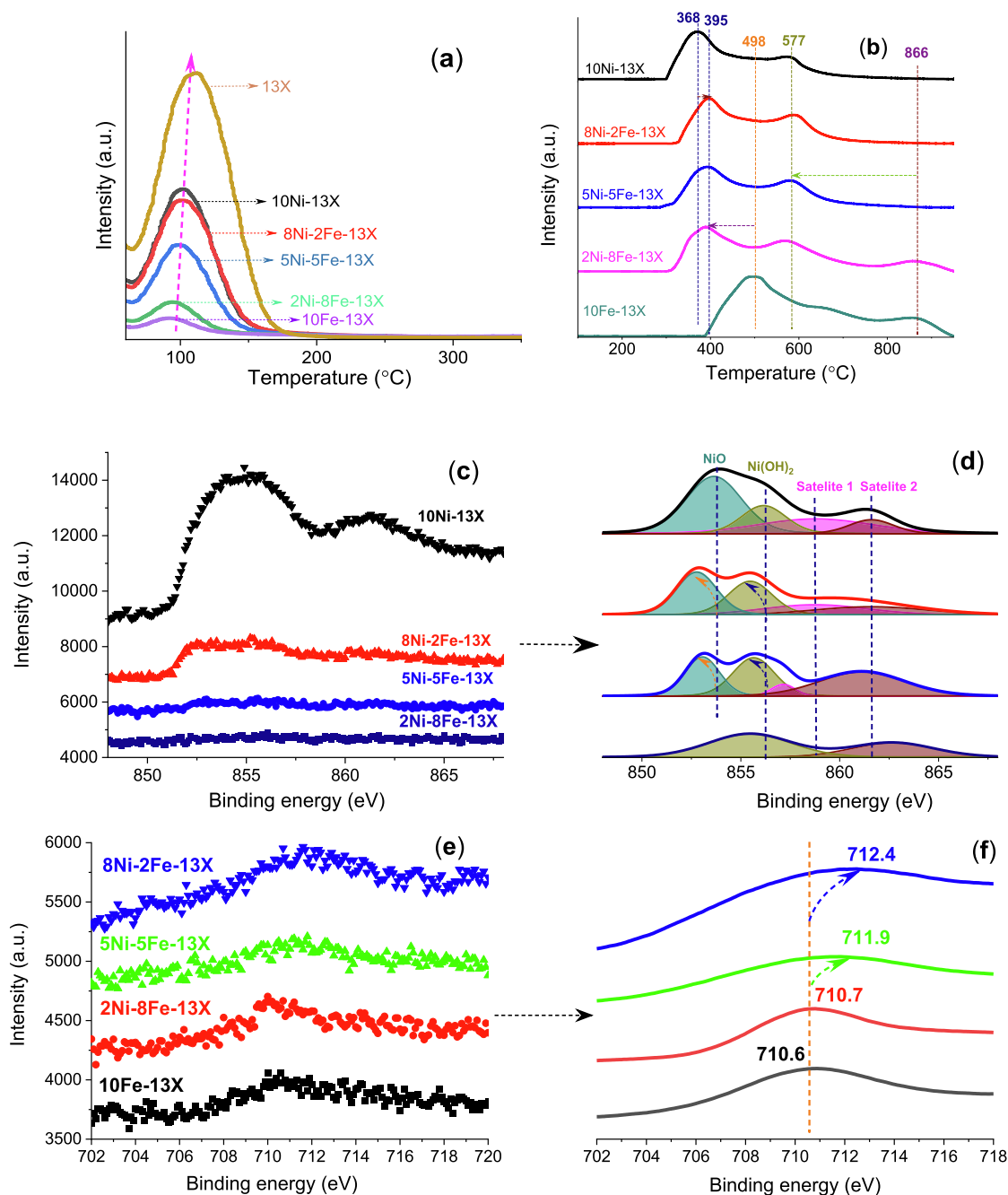
Fig. 2. (**a**) CO_2-TPD of reduced catalysts. (**b**) H_2-TPR profiles of the developed catalysts. (**c, d**) Ni $2p_{3/2}$ and (**e, f**) Fe $2p_{3/2}$ XPS spectra of Ni-Fe/13X samples.

highest CO_2 conversion (64.7 %) and methane selectivity (94.7 %) at 350 °C, indicating superior CO_2 methanation activity among the prepared catalysts. While 8Ni-2Fe-13X shows a comparable CO_2 conversion (~44 %) with that of 5Ni-5Fe-13X at 350 °C, its methane selectivity (78.2 %) is higher than that of 5Ni-5Fe-13X (71.0 %). The introduction of Fe species diminishes CO_2 methanation activity but yields a higher CO selectivity, suggesting that Ni-Fe species possess lower hydrogenation activity. This aligns with our prior investigations, where we found that Ni-Fe species displayed a reduced hydrogenation activity compared to monometallic Ni species [3]. The application of a higher reaction temperature (400 °C) resulted in a slight increase in the CO_2 conversion and CH_4 selectivity of the Ni-13X catalyst (Fig. 3b). However, a significant improvement in CO_2 methanation activity was observed with the 8Ni-2Fe-13X, 5Ni-5Fe-13X, and 2Ni-8Fe-13X catalysts at this higher temperature. This can be ascribed to the elevated hydrogenation activity of

bulk Ni species, which becomes activated at 350 °C. Conversely, the smaller Ni species and Ni-Fe exhibit a reduced hydrogenation activity at lower temperature. The performance results at GHSV of 60,000 mL h^{-1}·g$_{cat}^{-1}$ are illustrated in Figure S3. The depicted trend aligns with the analysis presented above. Some repeated experiments were conducted, and the results are presented in Table S1. These results indicate a low experimental error range of 0.3–2.5 %.

Notably, 5Ni-5Fe-13X and 2Ni-8Fe-13X catalysts both resulted in the formation of ethane. At 350 °C, 5Ni-5Fe-13X shows higher ethane selectivity than 2Ni-8Fe-13X (Fig. 3a). However, 2Ni-8Fe-13X demonstrates distinct ethane selectivity at 400 °C (Fig. 3b), while ethane formation is nearly absent in 5Ni-5Fe-13X. This result indicates high reaction temperatures promote hydrogenation activity of Ni species over 5Ni-5Fe-13X catalyst, favouring the CO methanation. Moreover, higher reaction temperature also favours the FTS reaction over the Fe domain
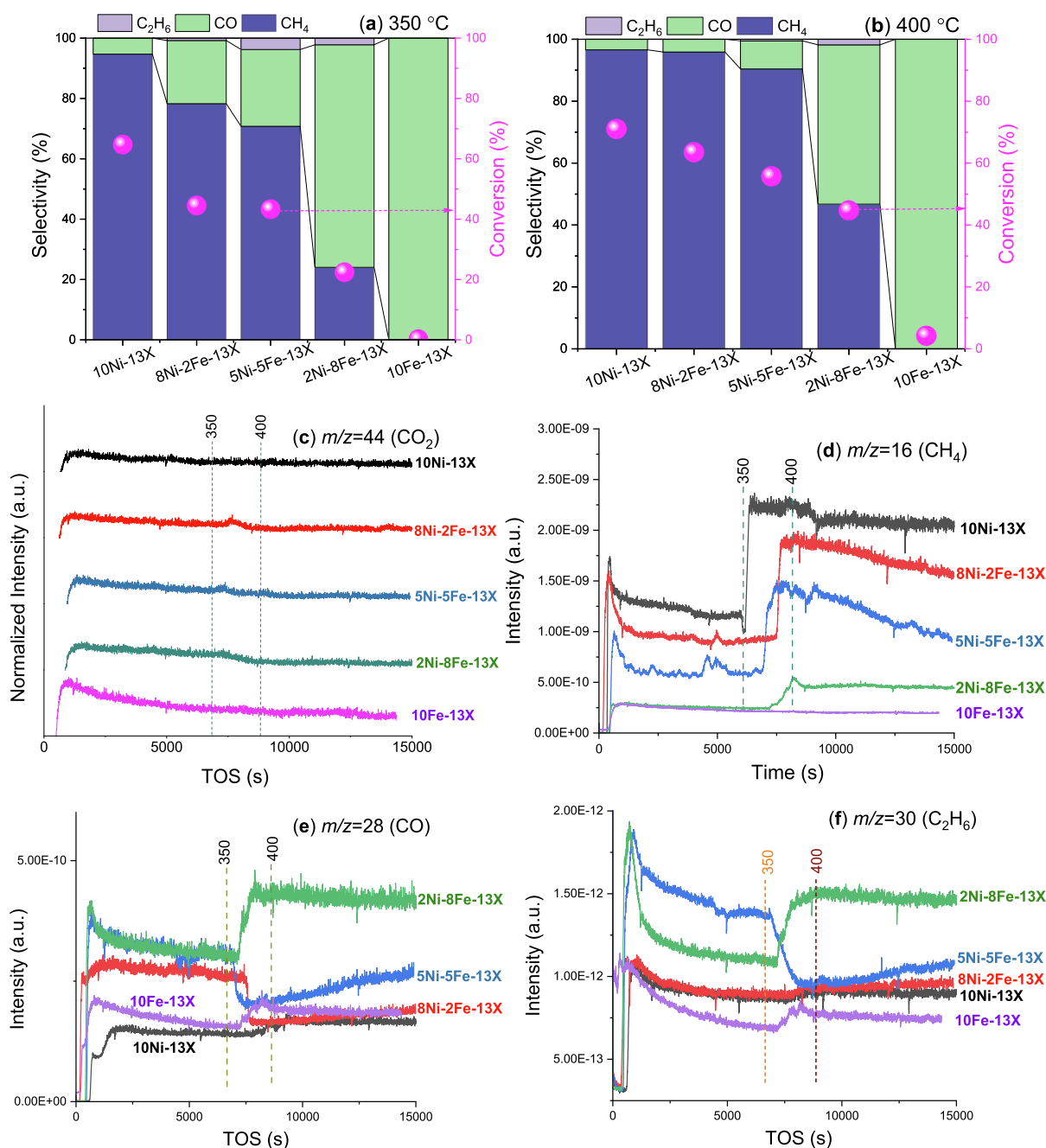
Fig. 3. CO_2 conversion and product selectivity at (**a**) 350 °C and (**b**) 400 °C, respectively. The conversion was measured 60 min after the start of each reaction temperature. The intensity of (**c**) CO_2 ($m/z = 44$), (**d**) CH_4 ($m/z = 16$), (**e**) CO ($m/z = 28$) and (**f**) C_2H_6 ($m/z = 30$) with time-on-stream (TOS) as measured by in situ mass spectrometry. Reaction conditions: H_2: 80 mL/min, CO_2: 20 mL/min, catalyst mass: 0.2 g.

catalyst, favouring the formation of CO and C_2H_6.

The online mass spectrometry results reveal a consistent trend: the intensity of CO_2 ($m/z = 44$) decreases as the reaction temperature increases from 350 to 400 °C, indicative of the consumption of CO_2. Methane intensity ($m/z = 16$) rises across all catalysts, suggesting heightened CO_2 methanation activity at higher temperatures. Concurrently, 2Ni-8Fe-13X displays elevated CO ($m/z = 28$) and C_2H_6 ($m/z = 30$) intensities as the reaction temperature increased from 350 to 400 °C. In contrast, 5Ni-5Fe-13X and 8Ni-2Fe-13X catalysts show decreased intensities of CO and C_2H_6, attributing to the increased CO methanation activity.

Notably, 8Ni-2Fe-13X, and 5Ni-5Fe-13X exhibit reduced methane intensity and increased CO intensity over time-on-stream, indicating a

diminished stability. The high stability of 10Ni-13X catalyst could be attributed to the low concentration of CO product, which traditionally favours the formation of surface carbon and thus leads to catalyst deactivation.

While the 2Ni-8Fe-13X catalysts exhibits a decreased hydrogenation activity, it shows a strong FTS activity. The weakened hydrogenation activity could be ascribed to its low content of Ni species, which are the main active sites for hydrogenation [41,66,67]. The small Ni particles promote the hydrogenation of CO_2 to CO. Subsequently, the H_2 and CO undergoes the FTS reaction to form ethane.

3.3. In situ DRIFTS analysis

To elucidate the reaction pathways and intermediates involved in CO_2 methanation, we conducted in situ DRIFTS analysis on two catalysts: 10Ni-13X and 2Ni-8Fe-13X, using a $CO_2/H_2 = 4$ mixture feed gas. Fig. 4a-c depict the evolution of IR spectra with increasing temperature during CO_2 methanation over 10Ni-13X, with corresponding results for 2Ni-8Fe-13X presented in Fig. 4d-f.

Notably, the CH_4 vibration (3015 cm^{-1}) [68,69] emerges at a relatively low temperature of 250 °C for 10Ni-13X (Fig. 4c), whereas this signal is detected at 300 °C for 2Ni-8Fe-13X (Fig. 4f). This observation underscores the superior CO_2 methanation activity of 10Ni-13X compared to 2Ni-8Fe-13X. Consistently, performance tests in the continuous-flow reactor reveal that the addition of Fe species diminishes the CO_2 methanation activity of Ni species, corroborating these findings.

The bands observed at 1913 cm^{-1} and 1907 cm^{-1} over 2Ni-8Fe-13X (Fig. 4e) are likely attributed to bridged carbonyl species [36,57,70]. Meanwhile, the band at 1525 cm^{-1}, prominently seen at 300 °C with the 10Ni-13X catalyst (Fig. 4a), is associated with HCOO* [71]. These findings suggest that CO* species are favored by Ni-Fe species, whereas the formation of HCOO* species is promoted by Ni alone. Subsequently, the HCOO* species undergo hydrogenation to form CH_4, while CO* is dissociated from the Ni-Fe species to produce CO. These observations are consistent with the results of flow reactor tests, demonstrating that Ni-Fe promotes the formation of CO and CH_4, whereas Ni species facilitate CH_4 formation. Additionally, the minor bands at 2871 cm^{-1} [72] and 2894 cm^{-1} [55,73] observed at Fig. 4e are attributed to the C-H stretching vibrations of methyl groups on alkylidene/methylidene species, suggesting the potential for hydrocarbon chain growth. This aligns with the presence of C_2H_6 observed in the flow reaction, which is promoted by Fe-rich species [74]. In addition, a small band at 1854 cm^{-1} was detected at a high reaction temperature (300 °C) over the 10Ni-13X catalyst (Fig. 4b), which can be attributed to CO* species [75]. This indicates that high reaction temperatures promote CO* reaction pathways to form CH_4.

Fig. 5 illustrates the reaction pathways for the conversion of CO_2 to CO, CH_4, and C_2H_6 over Ni and Ni-Fe species based on both our experimental findings and relevant literature [76–80], Initially, CO_2 undergoes hydrogenation to produce HCOO*, a process facilitated by Ni-domain species. The subsequent hydrogenation of HCOO* to CH_4 takes place with the assistance of spillover hydrogen provided by the Ni nanoparticles present on the 10Ni-13X, 8Ni-2Fe-13X, and 5Ni-5Fe-13X catalysts.

In contrast, the 2Ni-8Fe-13X demonstrates a diminished hydrogenation activity, leading to a heightened selectivity for CO. Remarkably, these CO species undergo FTS reaction, resulting in the formation of C_2H_6 over the 5Ni-5Fe-13X and 2Ni-8Fe-13X catalysts. It is noteworthy that the coupling reaction is favoured over the 5Ni-5Fe-13X catalyst at lower reaction temperature (350 °C), where the hydrogenation function of Ni species is constrained. In contrast, the 2Ni-8Fe-13X promotes the FTS for C_2H_6 formation at higher reaction temperatures (400 °C), as illustrated in Fig. 3f. The monometallic Fe species exhibit nearly negligible CO_2 conversion, indicating a notably weak hydrogenation activity of the Fe species.

It has been reported that adding Fe to Ni enhances CO_2 conversion (approximately 70 %) and CH_4 production (95 %) at 350 °C [68,81]. However, it should be noted that their studies used significantly higher Ni loading (~20 wt%) and a considerably more dilute feed gas ($H_2/CO_2/N_2$ vol.% = 64/16/20). The bulk Ni particles promote CO_2 methanation activity at lower temperatures. In contrast, we maintain constant total metal contents in this study, which differs from the previous studies. Keeping the total metal loading constant is a reasonable approach when investigating the influence of promoters on catalytic activity. In this study, both the flow reaction and the *in-situ* DRIFTS studies confirm that adding Fe to Ni/BEA reduces CO_2 methanation activity. The decreased hydrogenation activity of Ni-Fe species may promote CO formation pathways, leading to direct CO production without further hydrogenation.
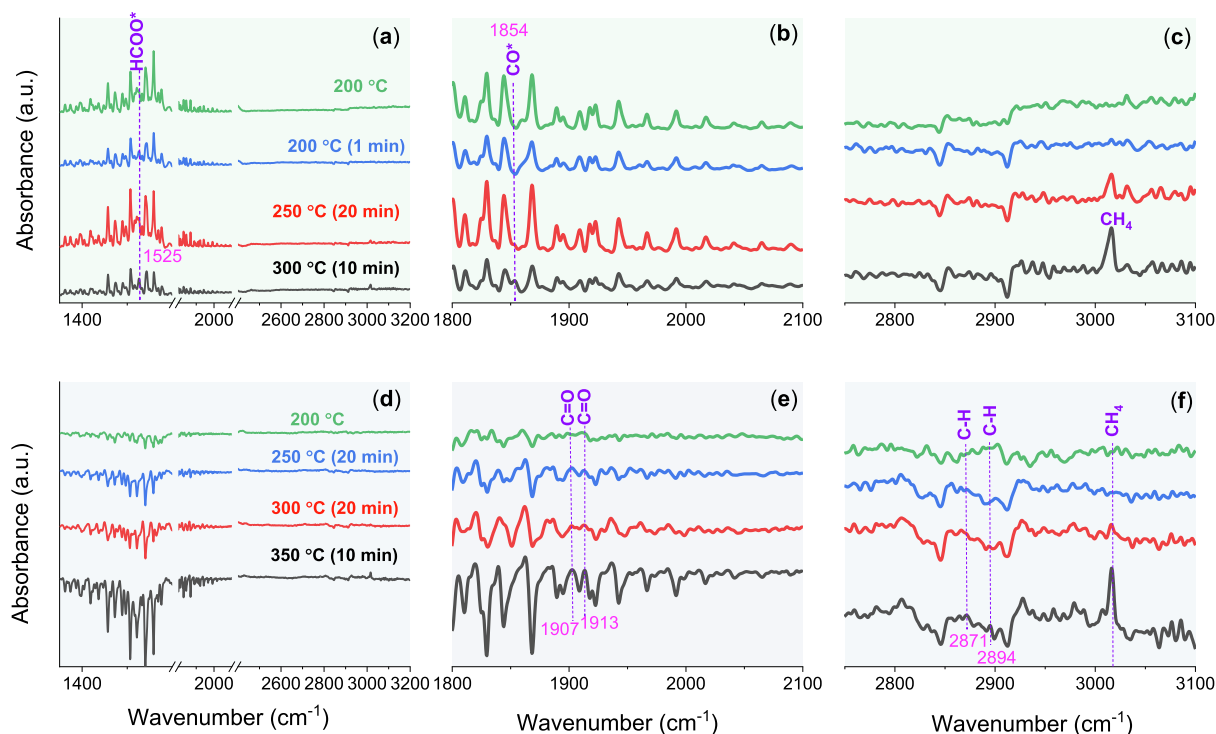
Fig. 4. In situ DRIFTS spectra of (**a-c**) 10Ni-13X and (**d-f**) 2Ni-8Fe-13X catalysts under CO_2 methanation conditions ($CO_2/H_2 = 1/4$) at increasing temperatures. The catalysts were reduced online at 500 °C for 2 h.
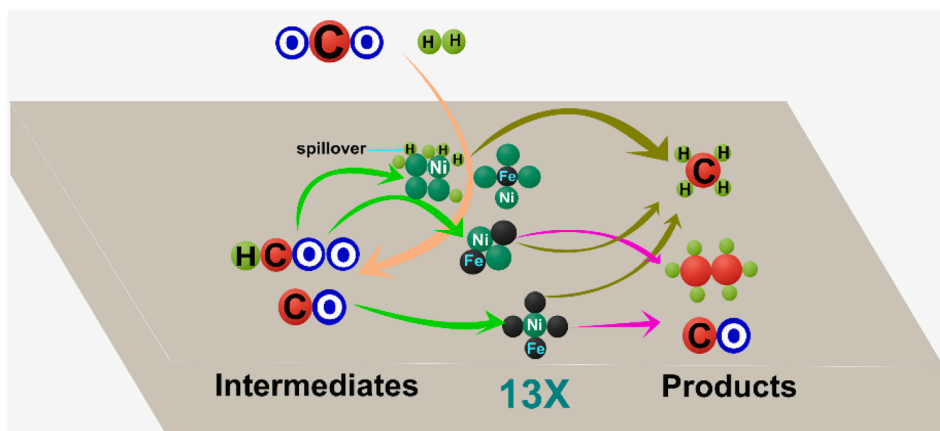
Fig. 5. Proposed pathways for hydrogenation of CO_2 to CO, CH_4, and C_2H_6 over 10Ni-13X, 8Ni-2Fe-13X, and 5Ni-5Fe-13X and 2Ni-8Fe-13X catalysts.

3.4. Long-term performance and spent catalyst characterization

The catalyst stability of 10Ni/13X in CO_2 methanation was investigated, and the results are illustrated in Fig. 6a. Notably, the 10Ni/13X catalyst exhibits commendable stability, with a slight decrease in CO_2 conversion from 82.3 % at 180 min to 78.8 % at the conclusion of the study (2970 min). The test results before 180 min were removed due to the adsorption of CO_2 by the dry silica gel in the beginning of the reaction. Particularly noteworthy is the observation that CO_2 conversion remains consistently high from 810 min to 2970 min, indicating excellent stability. Subsequent characterization of the spent 10Ni/13X catalyst using ATR-FTIR (Fig. 6b) and N_2 adsorption/desorption (Fig. 6c) revealed significant changes. A lengthier test lasting 8800 min was conducted, and its results are depicted in Figure S4. The test demonstrated remarkable stability, with CO_2 conversion decreasing by only 5 % from 180 min to the end.
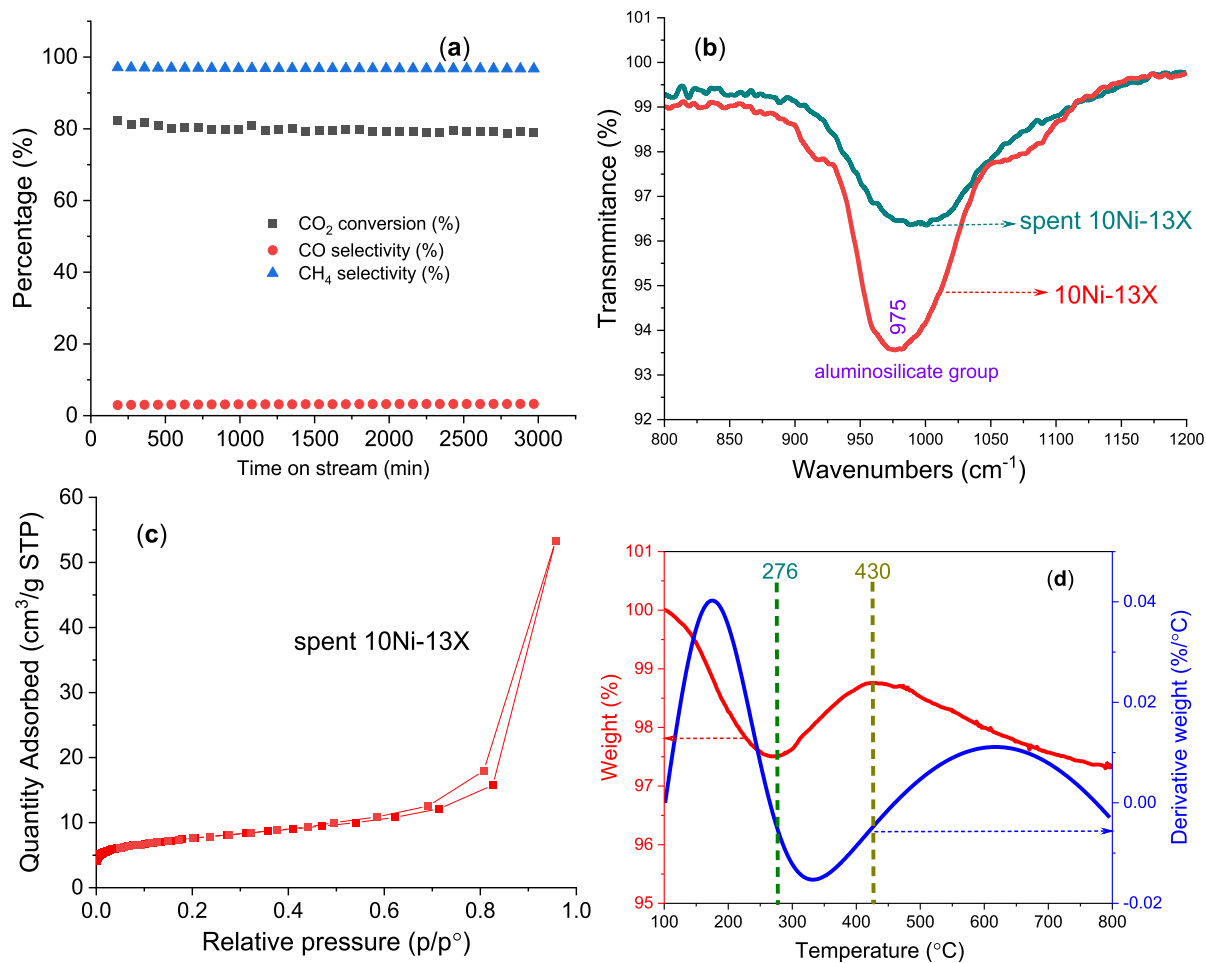
Fig. 6. (**a**) CO_2 conversion and selectivity of CO and CH_4 over 10Ni-13X catalyst during time on stream at 400 °C. Reaction conditions: 100 mL/min of mixture gas (19 % CO_2, 4 % N_2, 77 % H_2), catalyst mass: 0.25 g. (**b**) ATR-FTIR spectra of fresh and spent 10Ni-13X catalysts. (**c**) N_2 adsorption/desorption of spent 10Ni-13X catalyst. (**d**) TGA profile of the spent 10Ni-13X catalyst.

The band at 975 cm^{-1} in the ATR-FTIR spectrum can be attributed to the Si-O stretching vibrations of 13X zeolite [82]. Comparative analysis between the fresh 10Ni-13X and the spent 10Ni-13X indicates a marked reduction in intensity, attributed to carbon deposition in the zeolite. Additionally, the spent 10Ni-13X (Fig. 6c, Table S2) exhibits a substantial decrease in micropore surface area (8 m^2/g) compared to that of fresh one (354 m^2/g) (Fig. 1a, Table 1). This reduction suggests that the micropores were significantly blocked by deposited carbon. The analysis of the spent 10Ni-13X catalyst was further conducted through Thermogravimetric Analysis (TGA), and the outcomes are presented in Fig. 6d. After drying the spent catalyst at 100 °C for 30 min to eliminate moisture, significant observations were made. A conspicuous decrease in mass is evident from 100 to 276 °C, attributed to the presence of active carbonaceous species [83]. Furthermore, an increase in mass is noted from 276 to 430 °C, signifying the re-oxidization of metallic Ni species to NiO, resulting in an augmented catalyst mass. Subsequently, a mass decrease is observed from 430 to 800 °C, which can be linked to less active carbon content [84–86]. These findings collectively point towards a substantial deposition of carbon in the spent catalyst during CO$_2$ methanation.

Despite almost complete blockage of micropores by the deposited carbon, the catalyst exhibited no noticeable decrease in performance from 810 to 3000 min. This observation implies that the metals within the micropores play a negligible role in CO$_2$ methanation. In essence, the Ni species on the external surface emerge as the primary contributors to the catalytic activity in CO$_2$ methanation. This is in agreement with our previous study [17], which indicates that bulk Ni species on the external surface or within mesopores play a crucial role in CO$_2$ methanation.

4. Conclusions

This study delves into the structures of Ni-Fe species over Ni-Fe/13X with varying Ni/Fe ratios and examined their CO$_2$ methanation activity. The findings unveils the electronic interactions between Ni and Fe particles, resulting in electron transfer from Fe to Ni within the Ni-Fe species. Additionally, the formation of Ni-Fe species has a minor impact on the reduction temperature of Ni, while significantly lowering the reduction temperature of Fe oxides.

The established Ni-Fe species exhibits a diminished hydrogenation activity compared to the monometallic Ni species, leading to a reduced CO$_2$ conversion and CH$_4$ selectivity. The monometallic 10Ni-13X also exhibits robust stability, attributed to its high hydrogenation activity, which facilitates the conversion of CO to CH$_4$ and consequently inhibited the formation of surface-deposited carbon. We also demonstrated through in situ DRIFTS analysis that the 10Ni-13X catalyst exhibited higher CO$_2$ methanation activity compared to the bimetallic 2Ni-8Fe-13X catalyst. The Ni species promoted the formation of HCOO*, while the Ni-Fe species facilitated the CO* reaction pathways.

CRediT authorship contribution statement

Penghui Yan: Writing – original draft, Investigation, Formal analysis, Data curation, Conceptualization. **Hong Peng:** Writing – review & editing, Supervision, Project administration, Funding acquisition, Conceptualization. **Xi Zhang:** Writing – review & editing, Investigation, Data curation. **Hesamoddin Rabiee:** Writing – review & editing, Formal analysis, Data curation. **Mohamed Ahmed:** Writing – review & editing, Investigation, Data curation. **Yilun Weng:** Writing – review & editing, Investigation, Formal analysis, Data curation. **Alexandra Rozhkovskaya:** Writing – review & editing, Resources. **John Vogrin:** Writing – review & editing, Resources. **Muxina Konarova:** Writing – review & editing, Formal analysis, Data curation. **Zhonghua Zhu:** Writing – review & editing, Supervision, Project administration, Funding acquisition, Conceptualization.

References

[1] Xie B, Wong RJ, Tan TH, Higgam M, Gibson EK, Decarolis D, et al. Synergistic ultraviolet and visible light photo-activation enables intensified low-temperature methanol synthesis over copper/zinc oxide/alumina. Nature Commun 2020;11: 1615.

[2] Xie B, Tan TH, Kalantar-Zadeh K, Zheng J, Kumar P, Jiang J, et al. Promoting low-temperature methanol production over mixed oxide supported Cu catalysts: Coupling ceria-promotion and photo-activation. Appl Catal B Env 2022;315: 121599.

[3] Yan P, Kennedy E, Zhang H, Stockenhuber M. Catalytic hydropyrolysis of lignocellulosic biomass to BTX and biofuels over zeolite beta based catalysts. Fuel 2023;332:125946.

[4] Mesa-Jimenez JJ, Tzianoumis AL, Stokes L, Yang Q, Living VN. Long-term wind and solar energy generation forecasts, and optimisation of Power Purchase Agreements. Energy Rep 2023;9:292–302.

[5] Farsi S, Olbrich W, Pfeifer P, Dittmeyer R. A consecutive methanation scheme for conversion of CO$_2$ – A study on Ni$_3$Fe catalyst in a short-contact time micro packed bed reactor. Chem Eng J 2020;388:124233.

[6] Sabatier P, Senderens J. Direct hydrogenation of oxides of carbon in presence of various finely divided metals. CR Acad Sci 1902;134:689–91.

[7] Renda S, Ricca A, Palma V. Precursor salts influence in Ruthenium catalysts for CO$_2$ hydrogenation to methane. Appl Energy 2020;279:115767.

[8] Yarbas T, Ayas N. A detailed thermodynamic analysis of CO$_2$ hydrogenation to produce methane at low pressure. Int J Hydrogen Energy 2024;49:1134–44.

[9] Rui N, Zhang X, Zhang F, Liu Z, Cao X, Xie Z, et al. Highly active Ni/CeO$_2$ catalyst for CO$_2$ methanation: Preparation and characterization. Appl Catal B: Env 2021; 282:119581.

[10] Ahn JY, Chang SW, Lee SM, Kim SS, Chung WJ, Lee JC, et al. Developing Ni-based honeycomb-type catalysts using different binary oxide-supported species for synergistically enhanced CO$_2$ methanation activity. Fuel 2019;250:277–84.

[11] Yu J, Feng B, Liu S, Mu X, Lester E, Wu T. Highly active Ni/Al$_2$O$_3$ catalyst for CO$_2$ methanation by the decomposition of Ni-MOF@Al$_2$O$_3$ precursor via cold plasma. Appl Energy 2022;315:119036.

[12] Grange P. Catalytic hydrodesulfurization. Catal Rev Sci Eng 1980;21:37–41.

[13] Fan WK, Tahir M. Recent trends in developments of active metals and heterogenous materials for catalytic CO$_2$ hydrogenation to renewable methane: A review. J Env Chem Eng 2021;9:105460.

[14] Beierlein D, Haussermann D, Pfeifer M, Schwarz T, Stowe K, Traa Y, et al. Is the CO$_2$ methanation on highly loaded Ni-Al$_2$O$_3$ catalysts really structure-sensitive? Appl Catal B: Env 2019;247:200–19.

[15] Cui Y, Chen B, Xu L, Chen M, Wu C, Qiu J, et al. CO$_2$ methanation over the Ni-based catalysts supported on the hollow ZSM-5 zeolites: Effects of the hollow structure and alkaline treatment. Fuel 2023;334:126783.

[16] Kesavan JK, Luisetto I, Tuti S, Meneghini C, Lucci G, Battocchio C, et al. Nickel supported on YSZ: The effect of Ni particle size on the catalytic activity for CO$_2$ methanation. J CO2 Utilization 2018;23:200–11.

[17] Yan P, Peng H, Wu X, Rabiee H, Weng Y, Konarova M, et al. Impact of varied zeolite materials on nickel catalysts in CO$_2$ methanation. J Catal 2024;432:115439.

[18] Yan P, Peng H, Vogrin J, Rabiee H, Zhu Z. Selective CO$_2$ hydrogenation over zeolite-based catalysts for targeted high-value products. J Mater Chem A 2023;11: 17938–60.

[19] Baysal Z, Kureti S. CO$_2$ methanation on Mg-promoted Fe catalysts. Appl Catal B: Env 2020;262:118300.

[20] Kirchner J, Anolleck JK, Losch H, Kureti S. Methanation of CO2 on iron based catalysts. Appl Catal B: Env 2018;223:47–59.

[21] Franken T, A.. Heel, Are Fe based catalysts an upcoming alternative to Ni in CO2 methanation at elevated pressure? J CO2 Utilization 2020;39:101175.

[22] Paalanen PP, Weckhuysen BM. Carbon pathways, sodium-sulphur promotion and identification of iron carbides in iron-based fischer-tropsch synthesis. ChemCatChem 2020;12:4202–23.

[23] Li YT, Zhou L, Cui WG, Li ZF, Li W, Hu TL. Iron promoted MOF-derived carbon encapsulated NiFe alloy nanoparticles core-shell catalyst for CO2 methanation. J CO2 Utilization 2022;62:102093.

[24] Makdee A, Kidkhunthod P, Poo-arporn Y, Chanapattharapol KC. Enhanced CH4 selectivity for CO2 methanation over Ni-TiO2 by addition of Zr promoter. J Environ Chem Eng 2022;10:107710.

[25] Chen X, Ullah ST, Ye R, Jin C, Hu H, Hu F, Peng Y, Lu Z, Feng G, Zhou L, Zhang R. Insights into the Zn promoter for improvement of Ni/SiO2 catalysts prepared by the ammonia evaporation method toward CO2 methanation. Energy Fuels 2023;37: 3865–74.

[26] Le TA, Kim J, Kang JK, Park ED. CO and CO2 methanation over M (M=Mn, Ce, Zr, Mg, K, Zn, or V)-promoted Ni/Al@Al2O3 catalysts. Catal Today 2020;348:80–8.

[27] Quindimil A, De-La-Torre U, Pereda-Ayo B, González-Marcos JA, González-Velasco JR. Ni catalysts with La as promoter supported over Y- and BETA- zeolites for CO2 methanation. Appl Catal B: Env 2018;238:393–403.

[28] Aksoylu AE, Misirli Z, Onsan Z. Interaction between nickel and molybdenum in Ni–Mo/Al2O3 catalysts: I: CO2 methanation and SEM-TEM studies. Appl Catal A: Gen 1998;168:385–97.

[29] Summa P, Samojeden B, Motak M, Wierzbicki D, Alxneit I, Swierczek K, et al. Investigation of Cu promotion effect on hydrotalcite-based nickel catalyst for CO2 methanation. Catal Today 2022;384–386:133–45.

[30] Dias YR, Perez-Lopez OW. Carbon dioxide methanation over Ni-Cu/SiO2 catalysts. Energy Convers Manage 2020;203:112214.

[31] Summa P, Costa KSD, Wang Y, Samojeden B, Ronning M, Hu C, et al. Effect of cobalt promotion on hydrotalcite-derived nickel catalyst for CO2 methanation. Appl Mater Today 2021;25:101211.

[32] Guilera J, Valle JD, Alarcon A, Diaz JA, Andreu T. Metal-oxide promoted Ni/Al2O3 as CO2 methanation micro-size catalysts. J CO2 Utilization 2019;30:11–7.

[33] Hu F, Tong S, Lu K, Chen CM, Su FY, Zhou J, et al. Reduced graphene oxide supported Ni-Ce catalysts for CO2 methanation: The support and ceria promotion effects. J CO2 Utilization 2019;34:676–87.

[34] Ocampo F, Louis B, Kiwi-Minsker L, Roger AC. Effect of Ce/Zr composition and noble metal promotion on nickel based CexZr1−xO2 catalysts for carbon dioxide methanation. Appl Catal A: Gen 2011;392:36–44.

[35] Li M, Amari H, van Veen AC. Metal-oxide interaction enhanced CO2 activation in methanation over ceria supported nickel nanocrystallites. Appl Catal B: Env 2018; 239:27–35.

[36] Zhu M, Tian P, Cao X, Chen J, Pu T, Shi B, et al. Vacancy engineering of the nickel-based catalysts for enhanced CO2 methanation. Appl Catal B: Env 2021;282: 119561.

[37] Riani P, Valsamakis I, Cavattoni T, Escribano VS, Busca G, Garbarino G. Ni/SiO2-Al2O3 catalysts for CO2 methanation: Effect of La2O3 addition. Appl Catal B: Env 2021;284:119697.

[38] Ren J, Qin X, Yang JZ, Qin ZF, Guo HL, Lin JY, et al. Methanation of carbon dioxide over Ni–M/ZrO2 (M = Fe Co, Cu) catalysts: Effect of addition of a second metal. Fuel Process Technol 2015;137:204–11.

[39] Hwang S, Hong UG, Lee J, Baik JH, Koh DJ, Lim H, et al. Methanation of carbon dioxide over mesoporous nickel–M–alumina (M = Fe, Zr, Ni, Y, and Mg) xerogel catalysts: effect of second metal. Catal Lett 2012;142:860–8.

[40] Xu L, Cui Y, Chen M, Wen X, Lv C, Wu X, et al. Screening transition metals (Mn, Fe Co, and Cu) promoted Ni-Based CO2 methanation bimetal catalysts with advanced low-temperature activities. Ind Eng Chem Res 2021;60:8056–72.

[41] Yan P, Tian X, Kennedy EM, Tkachenko OP, Stockenhuber M. Influence of promoters (Fe, Mo, W) on the structural and catalytic properties of Ni/BEA for guaiacol hydrodeoxygenation. ACS Sustainable Chem Eng 2021;9:15673–82.

[42] Yan P, Kennedy E, Stockenhuber M. Hydrodeoxygenation of guaiacol over BEA supported bimetallic Ni-Fe catalysts with varied impregnation sequence. J Catal 2021;404:1–11.

[43] Andersson MP, Bligaard T, Kustov A, Larsen KE, Greeley J, Johannessen T, et al. Toward computational screening in heterogeneous catalysis: Pareto-optimal methanation catalysts. J Catal 2006;239:501–6.

[44] Bligaard T, Norskov JK, Dahl S, Matthiesen J, Christensen CH, Sehested J. The Brønsted–Evans–Polanyi relation and the volcano curve in heterogeneous catalysis. J Catal 2004;224:206–17.

[45] Pandey D, Deo G. Promotional effects in alumina and silica supported bimetallic Ni–Fe catalysts during CO2 hydrogenation. J Mol Catal A: Chem 2014;382:23–30.

[46] Wolf M, Wong LH, Schuler C, Hinrichsen O. CO2 methanation on transition-metal-promoted Ni-Al catalysts: Sulfur poisoning and the role of CO2 adsorption capacity for catalyst activity. J CO2 Utilization 2020;36:276–87.

[47] Mutz B, Belimov M, Wang W, Sprenger P, Serrer MA, Wang D, et al. Potential of an alumina-Supported Ni3Fe catalyst in the methanation of CO2: impact of alloy formation on activity and stability. ACS Catal 2017;7:6802–14.

[48] Pandey D, Deo G. Effect of support on the catalytic activity of supported Ni–Fe catalysts for the CO2 methanation reaction. J Ind Eng Chem 2016;33:99–107.

[49] Huynh HL, Tucho WM, Yu X, Yu Z. Synthetic natural gas production from CO2 and renewable H2: Towards large-scale production of Ni–Fe alloy catalysts for commercialization. J Clean Prod 2020;264:121720.

[50] Piano GD, Gamboa JJA, Condo AM, Bengio S, Gennari FC. Bimetallic Ni-Fe catalysts for methanation of CO2: Effect of the support nature and reducibility. Appl Catal A: Gen 2022;634:118540.

[51] Serrer MA, Kalz KF, Saraci E, Lichtenberg H, Grunwaldt JD. Role of Iron on the Structure and Stability of Ni3.2Fe/Al2O3 during Dynamic CO2 Methanation for P2X Applications. ChemCatChem 2019;11:5018–21.

[52] Yan B, Zhao B, Kattel S, Wu Q, Yao S, Su D, et al. Tuning CO2 hydrogenation selectivity via metal-oxide interfacial sites. J Catal 2019;374:60–71.

[53] Winter LR, Gomez E, Yan B, Yao S, Chen JG. Tuning Ni-catalyzed CO2 hydrogenation selectivity via Ni-ceria support interactions and Ni-Fe bimetallic formation. Appl Catal B: Env 2018;224:442–50.

[54] Reich R, Danisi RM, Kluge T, Eiche E, Kolb J. Structural and compositional variation of zeolite 13X in lithium sorption experiments using synthetic solutions and geothermal brine. Micro Meso Mater 2023;359:112623.

[55] Yan P, Tian X, Kennedy EM, Stockenhuber M. Advanced in situ IR spectroscopy study of anisole hydrodeoxygenation over Ni/SiO2 catalysts. J Catal 2023;427: 115102.

[56] Li Z, Liu J, Shi R, Waterhouse GIN, Wen XD, Zhang T. Fe-based catalysts for the direct photohydrogenation of CO2 to value-added hydrocarbons. Adv Energy Mater 2021;11:2002783.

[57] Zhang X, Xue L, Li J, Li M, Liu W, Su H, et al. Electrodeposited Ni–Fe alloy foils with changeable nanostructures and magnetic properties for high performance wireless charging. J Superconduct Novel Magnet 2023;36:1225–34.

[58] Gao Y, Zhao Z, Jia H, Yang X, Lei X, Kong X, et al. Partially reduced Ni2+, Fe3+-layered double hydroxide for ethanol electrocatalysis. J Mater Sci 2019;54: 14515–23.

[59] Yan P, Xi S, Peng H, Mitchell DRG, Harvey L, Drewery M, et al. Facile and eco-friendly approach to produce confined metal cluster catalysts. J Am Chem Soc 2023;145:9718–28.

[60] Yan P, Tian X, Kennedy EM, Stockenhuber M. The role of Ni sites located in mesopores in the selectivity of anisole hydrodeoxygenation, Catal. Sci Technol 2022;12:2184–96.

[61] Akri M, Zhao S, Li X, Zang K, Lee AF, Isaacs MA, et al. Atomically dispersed nickel as coke-resistant active sites for methane dry reforming. Nature Commun 2019;10: 5181.

[62] Goncalves LPL, Sousa JPS, Soares OSGP, Bondarchuk O, Lebedev OI, Kolenko YV, et al. The role of surface properties in CO2 methanation over carbon-supported Ni catalysts and their promotion by Fe. Catal Sci Technol 2020;10:7217.

[63] Zhu J, Wang P, Zhang X, Zhang G, Li R, Li W, et al. Dynamic structural evolution of iron catalysts involving competitive oxidation and carburization during CO2 hydrogenation. Sci Adv 2022;8:eabm3629.

[64] Frontera P, Macario A, Monforte G, Bonura G, Ferraro M, Dispenza G, et al. The role of gadolinia doped ceria support on the promotion of CO2 methanation over Ni and NiFe catalysts. Int J Hydrogen Energy 2017;42:26828–42.

[65] Hu S, He L, Wang Y, Su S, Jiang L, Chen Q, et al. Effects of oxygen species from Fe addition on promoting steam reforming of toluene over Fe-Ni/Al2O3 catalysts. Int J Hydrogen Energy 2016;41:17967–75.

[66] Wei L, Haije W, Kumar N, Peltonen J, Peurla M, Grenman H, et al. Influence of nickel precursors on the properties and performance of Ni impregnated zeolite 5A and 13X catalysts in CO2 methanation. Catal Today 2021;362:35–46.

[67] Wei L, Grenman H, Haije W, Kumar N, Aho A, Eranen K, et al. Sub-nanometer ceria-promoted Ni 13X zeolite catalyst for CO2 methanation. Appl Catal A: Gen 2021;612:118012.

[68] Huynh HL, Zhu J, Zhang G, Shen Y, Tucho WM, Ding Y, et al. Promoting effect of Fe on supported Ni catalysts in CO2 methanation by in situ DRIFTS and DFT study. J Catal 2020;392:266–77.

[69] Gonzalez-Castano M, Gonzalez-Arias J, Bobadilla LF, Ruiz-Lopez E, Odriozola JA, Arellano-Garcia H. In-situ DRIFTS steady-state study of CO2 and CO methanation over Ni-promoted catalysts. Fuel 2023;338:127241.

[70] Vrijburg WL, Garbarino G, Chen W, Parastaev A, Longo A, Pidko EA, et al. Ni-Mn catalysts on silica-modified alumina for CO2 methanation. J Catal 2020;382: 358–71.

[71] Goncalves LPL, Mielby J, Soares OSGP, Sousa JPS, Petrovykh DY, Lebedev OI, et al. In situ investigation of the CO2 methanation on carbon/ceria-supported Ni catalysts using modulation-excitation DRIFTS. Appl Catal B Env 2022;312:121376.

[72] Wang X, Hong Y, Shi H, Szanyi J. Kinetic modeling and transient DRIFTS–MS studies of CO2 methanation over Ru/Al2O3 catalysts. J Catal 2016;343:185–95.

[73] Moran JI, Alvarez VA, Cyras VP, Vazquez A. Extraction of cellulose and preparation of nanocellulose from sisal fibers. Cellul 2008;15:149–59.

[74] Badoga S, Martinelli M, Gnanamani MK, Koh Y, Shafer WD. New mechanism insight for the hydrogenation of CO/CO2 gas mixtures to hydrocarbons over iron-based catalyst. Catal Commun 2021;152:106284.

[75] Liu R, Leshchev D, Stavitski E, Juneau M, Agwara JN. Selective hydrogenation of CO2 and CO over potassium promoted Co/ZSM-5. Appl Catal B: Env 2021;284: 119787.

[76] Serrer MA, Gaur A, Jelic J, Weber S, Fritsch C, Clark AH, et al. Structural dynamics in Ni–Fe catalysts during CO2 methanation – role of iron oxide clusters, Catal. Sci Technol 2020;10:7542–54.

[77] Kikkawa S, Teramura K, Kato K, Asakura H, Hosokawa S, Tanaka T. Formation of CH4 at the Metal-Support Interface of Pt/Al2O3 During Hydrogenation of CO2: Operando XAS-DRIFTS Study. ChemCatChem 2022;14:e202101723.

[78] Cherevotan A, Raj J, Dheer L, Roy S, Sarkar S, Das R, et al. Operando Generated Ordered Heterogeneous Catalyst for the Selective Conversion of CO2 to Methanol. ACS Energy Lett 2021;6:509–16.

[79] Jia X, Zhang X, Rui N, Hu X, Liu CJ. Structural effect of Ni/ZrO2 catalyst on CO2 methanation with enhanced activity. Appl Catal B: Env 2019;244:159–69.

[80] Zhao J, Shi R, Waterhouse GIN, Zhang T. Selective photothermal CO_2 reduction to CO, CH_4, alkanes, alkenes over bimetallic alloy catalysts derived from layered double hydroxide nanosheets. Nano Energy 2022;102:107650.

[81] Dias YR, Perez-Lopez OW. CO_2 conversion to methane using Ni/SiO_2 catalysts promoted by Fe, Co and Zn. J Env Chem Eng 2021;9:104629.

[82] Boroglu MS, Gurkaynak MA. Fabrication and characterization of silica modified polyimide–zeolite mixed matrix membranes for gas separation properties. Polym Bull 2011;66:463–78.

[83] Zeng YX, Wang L, Wu CF, Wang JQ, Shen BX, Tu X. Low temperature reforming of biogas over K-, Mg- and Ce-promoted Ni/Al_2O_3 catalysts for the production of

hydrogen rich syngas: Understanding the plasma-catalytic synergy. Appl Catal B: Env 2018;224:469–78.

[84] Yan P, Azreena IN, Peng H, Rabiee H, Ahmed M, Weng Y, et al. Catalytic hydropyrolysis of biomass using natural zeolite-based catalysts. Chem Eng J 2023; 476:146630.

[85] Juan-Juan J, Roman-Martinez MC, Illan-Gomez MJ. Effect of potassium content in the activity of K-promoted Ni/Al_2O_3 catalysts for the dry reforming of methane. Appl Catal A: Gen 2006;301:9–15.

[86] Nandini A, Pant KK, Dhingra SC. K-, CeO_2-, and Mn-promoted Ni/Al_2O_3 catalysts for stable CO_2 reforming of methane. Appl Catal A: Gen 2005;290:166–74.